Improved range estimation using simple infrared sensors without prior knowledge of surface characteristics

Çağrı Yüzbaşıoğlu and Billur Barshan

Department of Electrical Engineering, Bilkent University, TR-06800 Bilkent, Ankara, Turkey

E-mail: cagri@ee.bilkent.edu.tr and billur@ee.bilkent.edu.tr

Abstract
This paper describes a new method for position estimation of planar surfaces using simple, low-cost infrared sensors. The intensity data acquired with infrared sensors depend highly on the surface properties and the configuration of the sensors with respect to the surface. Therefore, in many related studies, either the properties of the surface are determined first or certain assumptions about the surface are made in order to estimate the distance and the orientation of the surface relative to the sensors. We propose a novel method for position estimation of surfaces with infrared sensors without the need to determine the surface properties first. The method is considered to be independent of the type of surface encountered since it is based on searching for the position of the maximum value of the intensity data rather than using absolute intensity values which would depend on the surface type. The method is verified experimentally with planar surfaces of different surface properties. An intelligent feature of our system is that its operating range is made adaptive based on the maximum intensity of the detected signal. Three different ways of processing the intensity signals are considered for range estimation. The absolute mean range error for the method resulting in the lowest errors is 0.15 cm over the range from 10 to 50 cm. The cases where the azimuth and elevation angles are nonzero are considered as well. The results obtained demonstrate that infrared sensors can be used for localization to an unexpectedly high accuracy without prior knowledge of the surface characteristics.

Keywords: infrared sensors, Phong illumination model, position estimation, range measurement, surface localization, optical sensing

(Some figures in this article are in colour only in the electronic version)

1. Introduction

An important task for many intelligent autonomous systems exploring their environment is to estimate the positions of surrounding objects as accurately as possible. Ultrasonic and infrared sensors are simple, commonly employed, and relatively low-cost sensing modalities to perform this task. Infrared sensors may be preferable to ultrasonic sensors due to their faster response time, narrower beamwidth and lower cost. Typically, infrared sensors are used as a pair, one as an emitter and the other as a detector. The emitted light reflected from the surface is detected by the detector. The intensity of the light detected depends on several parameters including the surface reflectance properties, the distance to the surface, and the relative orientation of the emitter, the detector and the surface. Consequently, one problem with the use of infrared sensors for position estimation is that single intensity readings are often not reliable enough to make sufficiently accurate range estimates since they are highly affected by the properties of the reflecting surface.

Conversely, it is not possible to deduce the surface properties of the reflector based on a single intensity return without knowing its position and orientation, because the reflected light depends highly on the distance and the angular orientation of the reflecting surface. Due to single intensity readings not providing sufficiently accurate information about an object's position and properties, the recognition capabilities of simple infrared sensors have been underestimated and underused in many applications. Although these devices are inexpensive, practical and widely available, their use has been mostly limited to the detection of the presence or absence of objects in the environment (proximity detection) for applications such as obstacle avoidance or counting. Gathering further information about objects with simple infrared sensors has not been investigated in depth. However, due to the limited resources of intelligent autonomous systems, the available resources need to be used as much as possible. This means that the ability of simple sensor systems to extract information about the environment should first be maximally exploited before more expensive sensing modalities with higher resolution and higher resource requirements (such as computing power) are considered for a given task. Therefore, one of the aims of this study is to explore the limits of simple and inexpensive infrared sensors for accurate position estimation in order to extend their usage to tasks beyond simple proximity detection.

One solution to the above-stated problem is to employ infrared sensors in conjunction with other sensing modalities to acquire information about the surface properties of the object so that the accuracy of range estimates is improved. Such an approach is taken in [1, 2], where the surface parameters are determined before the range is estimated. In [1], the properties of planar surfaces at a known distance (measured by an ultrasonic sensor) have been determined first using the Phong illumination model [3]. Using this information, the infrared sensor can be employed as an accurate range finder for planar surfaces over the range from 5 to 23 cm. The largest error between 10 and 16 cm has been calculated as 0.2 cm, whereas for ranges lower than 10 cm, the error increases to about 0.6 cm. In [2], the infrared reflection coefficient of the surface is estimated according to a simplified reflection model first, using ultrasonic data as a complementary source of information. The range of operation of this system is between 10 and 100 cm with range errors varying from 0.1 mm for nearby objects to 10 cm for distant objects, being typically 1.2 cm for objects placed at 50 cm. A similar approach is taken in [4, 5] where colours are differentiated by employing infrared and ultrasonic sensors in a complementary fashion. Other researchers have also dealt with the fusion of information from infrared and ultrasonic sensors [6, 7] and infrared and radar systems [8, 9].

Infrared sensors have a wide variety of applications in safety and security systems, process control, robotics and automation, and remote sensing. Their most common use has been in relatively simple tasks such as simple object and proximity detection [10] and counting [11, 12]. Other applications are position measurement and control [13], map building [14] and machine vision systems [15]. In [10], infrared proximity sensing for a robot arm is discussed. Following this work, [16] describes a robot arm completely covered with an infrared skin sensor to detect nearby objects

and avoid collision. Infrared sensors are used in floor sensing, door detection [17], mapping of openings in walls [6, 18], as well as monitoring doors/windows of buildings and vehicles, and as 'light curtains' for protecting an area. In [19], an automated guided vehicle detects unknown obstacles by means of an 'electronic stick' consisting of infrared sensors, using a strategy similar to that adopted by a blind person. Papers [20–22] deal with the optical determination and monitoring of depth information. A number of commercially available infrared sensors are evaluated in [23] for space applications. Papers [24, 25] describe a passive multi-element infrared sensor array which identifies the locations of the people in a room using thermal imaging. Paper [26] deals with determining the range of a planar surface. By incorporating the optimal amount of additive noise in the infrared range measurement system, the authors were able to improve the system sensitivity and extend the operating range of the system. Infrared sensors have also been used for automated sorting of waste objects made of different materials [27, 28].

The use of infrared sensing in the pattern recognition area has been mostly limited to the recognition or detection of features or targets in conventional two-dimensional images. Examples of work in this category include face identification [29], automatic vehicle detection [30], automatic target recognition [31] and tracking [32], detection and identification of targets in background clutter [33, 34], remote sensing [35] and automated terrain analysis [36].

In our earlier works related to infrared sensing, we considered infrared sensors as the only sensing modality, and used multiple intensity readings in the form of angular intensity scans for the differentiation and localization of objects [37–39]. These works were based on a template-storage approach, which uses the distinctive nature of the infrared intensity scans. In [37], a correct classification rate of 97% was achieved with absolute range and azimuth errors of 0.8 cm and 1.6° for targets with different geometrical properties but made of the same surface material (unpolished wood). A rule-based approach to the same problem may be found in [40] where we achieve an average correct target differentiation rate of 91.3% over four target types with average absolute range and azimuth errors of 0.55 cm and 1.03°, respectively. The advantages of a rule-based approach are shorter processing time, minimal storage requirements, greater robustness to noise and deviations in geometry and surface properties, since the rule-based approach emphasizes structural features rather than the exact functional forms of the scans. In [38], targets made of different surface materials but of the same planar geometry are differentiated with a correct differentiation rate of 87% and absolute range and azimuth errors of 1.2 cm and 1.0°. In [39], we dealt with the problem of differentiating and localizing targets whose geometry and surface properties both vary, generalizing and unifying the results of [37, 38]. A correct classification rate of 80% of both geometry and surface over all target types considered is achieved and targets are localized within absolute range and azimuth errors of 1.5 cm and 1.1°, respectively. In [41], we considered a parametric approach based on estimating, storing and matching the parameters of angular scans according to an assumed reflection model. We achieved a correct differentiation rate of 100% for six surfaces and the surfaces

Figure 1. A closeup view of the infrared sensor.

Figure 2. The experimental set-up used in this study.

are localized within absolute range and azimuth errors of 0.2 cm and 1.1°, respectively. The differentiation rate decreases to 86% for seven surfaces and to 73% for eight surfaces. The main disadvantage of these methods is that they all rely on prior knowledge and require the storage of either the intensity scan templates or the parameters corresponding to the surface types or geometries to be differentiated.

In this study, we present an approach to position estimation which is relatively independent of surface type and does not require any prior information about the surface. We use a pair of infrared sensors (figure 1), one as emitter, and the other as detector, mounted on a vertical linear platform on which they can be moved independently along a straight line as shown in figure 2. Both sensors make a predetermined angle (γ) with the linear platform on which they slide. The basic idea of our method is that, while the sensors are being moved, the detector reading is maximum at some positions and the corresponding positional values of the sensors can be used for range estimation with suitable processing of the

infrared intensity scans. To realize this idea, for a given position of the emitter, the detector slides along the platform to collect intensity data and these data are compared to find the maximum in magnitude. The detector position corresponding to the maximum intensity data is recorded together with the corresponding *baseline separation*, which is the distance between the emitter and the detector. The distance to the surface is then estimated based on this information in a way which is relatively independent of surface type, as will be explained in more detail in section 2. In short, the system can be viewed as a variable triangulation system tuned to maximum intensity data. The reason that the linear platform stands vertically and not horizontally is that in many typical indoor environments, there is much less variation in depth in the vertical direction when compared to the horizontal and this configuration choice eliminates discontinuities in range along the direction of motion of the detector as much as possible.

Since the method is based on searching for the maximum value of the intensity rather than using absolute intensity values for a given surface (which would depend on the surface properties), it can be considered to be independent of the type of surface encountered. This is the main difference of our approach from the earlier attempts to estimate range with infrared sensors. However, the type of surface inevitably affects the range of distances over which intensity data are available from a surface and determines the operating range of the system. Therefore, one can say that as long as intensity data from a surface are available, range is estimated relatively independently of the surface type. Our results indicate that if the data acquired from such simple infrared sensors are processed effectively through the use of suitable techniques, substantially more information about the environment can be extracted with these devices than in their typical applications.

The organization of this paper is as follows. In section 2, the range estimation technique proposed in this study is described in detail. Experimental verification is provided in section 3 where details of the experimental set-up and the experimental results under different conditions are provided. Three different ways of processing the infrared intensity scans are considered and evaluated. In the final section, concluding remarks are made and directions for future research are indicated.

2. Position estimation

The method presented in this study is based on the Phong illumination model [3], frequently used in computer graphics applications. This model combines the three types of reflection, which are ambient, diffuse and specular reflection, in a single formula:

$$I = I_a k_a + I_i [k_d(\vec{l} \cdot \vec{n})] + I_i [k_s(\vec{t} \cdot \vec{v})^m] \quad (1)$$

Here, I_a and I_i are the intensities of ambient and incident light, k_a, k_d and k_s are the coefficients of ambient, diffuse and specular reflection for a given material, m is the specular fall-off factor, and $\vec{l}, \vec{n}, \vec{t}, \vec{v}$ are the unit vectors representing the direction of the light source, the surface normal, the reflected light and the viewing point, respectively, as shown in figure 3. In diffuse or Lambertian reflection, represented by the second term in equation (1), the incident light is scattered equally in all
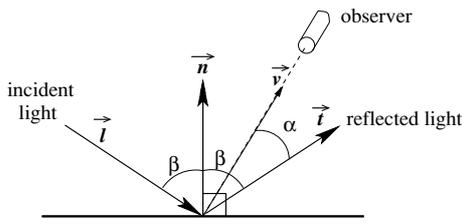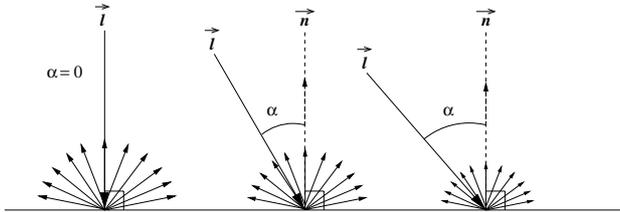
Figure 3. Specular reflection.

Figure 4. Diffuse reflection at different angles of incidence.

directions and the intensity of the scattered light is proportional to the cosine of the angle between the incident light and the surface normal (figure 4). This is known as Lambert's cosine law [42]. In specular reflection, represented by the last term in equation (1), light is reflected in only one direction such that the angle of incidence equals the angle of reflection (figure 3). In this study, the ambient reflection component, which is the first term in the above sum, is minimized, in fact zeroed by an infrared filter, covering the detector window. Therefore, the reflected intensity is a combination of diffuse and specular components.

The position and orientation of the surface with respect to the sensors are described in spherical coordinates using r (range), θ (azimuth angle) and ϕ (elevation angle) as shown in figure 5. Referring to the same figure, the *sensor plane* is the plane on which the emitter, the detector and their lines of sight lie. The *line of interest* is the intersection of the sensor plane with the surface, which is the line from which the distance is measured or calculated. Since the linear platform stands vertically in our case, it is important to detect whether ϕ equals zero or not as the first step. The cases for $\phi = 0°$ and $\phi \neq 0°$ are investigated separately in the following two subsections.

2.1. Surfaces with $\phi = 0°$

When ϕ is zero, since the line of interest and the sensor platform are parallel, all maximum intensity data for different positions of the emitter should be equal to each other within some given error tolerance. Also, measured baseline separations corresponding to the maximum intensity data should be equal to each other, again within some given error tolerance. Once it is detected that $\phi = 0°$, the next step is to determine θ. In fact, the value of θ is not needed for range estimation. To show this, let us first consider the simple case where ϕ and θ are both equal to zero.

2.1.1. $\phi = 0°, \theta = 0°$.
When ϕ and θ are both equal to zero, both specular and diffuse reflection components are detected. Due to specular reflection properties, the detector senses the maximum specular reflection component at position 1
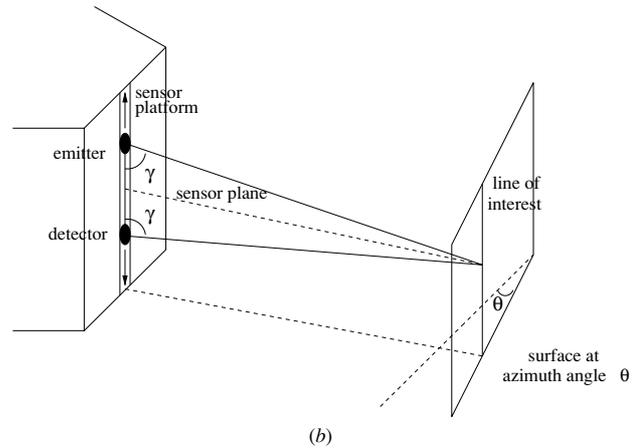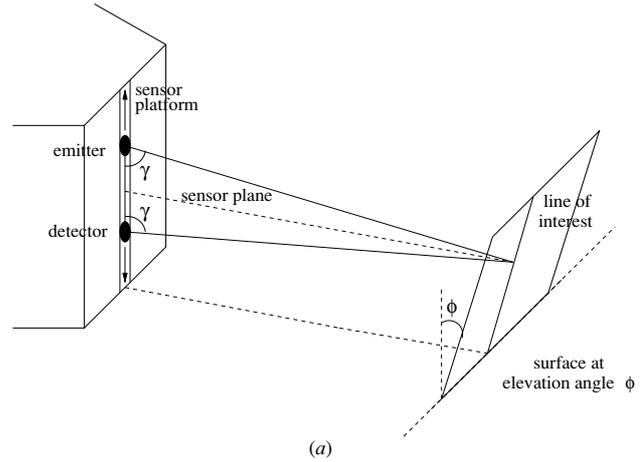

(a)

(b)

Figure 5. The general case where (a) $\phi \neq 0°$, and (b) $\theta \neq 0°$.

Figure 6. Sensing the specularly and diffusely reflected components.

where the distance a is adjusted such that the lines of sight of the emitter and detector meet at the point of reflection, and consequently, $\gamma + \psi = 90°$ (figure 6). Here, a is half of the baseline separation between the emitter and the detector when the detector senses the maximum intensity data and γ is the acute angle between the sensor line of sight and the linear platform. Although diffusely reflected light is scattered equally in all directions as shown in figure 6, the detector senses the diffuse reflection component maximally again at position 1 where there is a component of the reflection

Figure 7. Specularly reflected light propagating on a distinct plane when $\theta \neq 0°$.

Figure 8. Diffusely reflected light propagating on distinct planes.

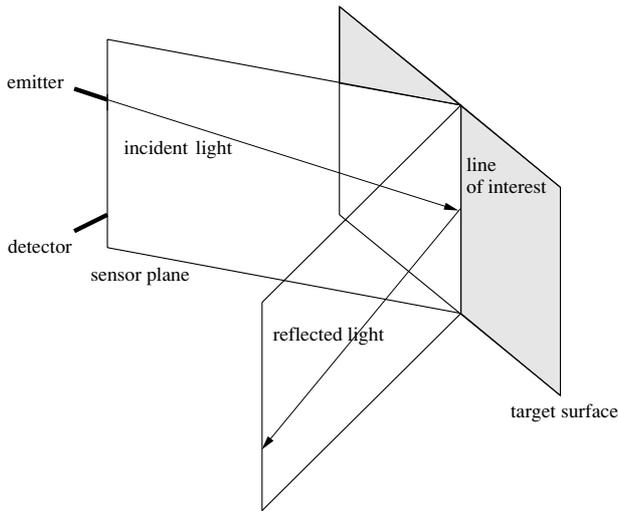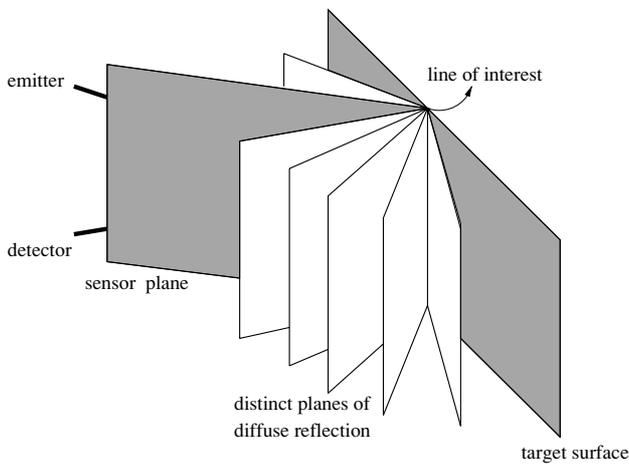in alignment with the detector line of sight. Therefore, diffuse and specular reflection components act the same way to maximize the detector reading when the emitter and the detector are equidistant from the surface normal. From the geometry of figure 6, the distance between the sensor platform and the line of interest is given by

$$r = a \tan \gamma \qquad (2)$$

Therefore, using the measured value of a and the known value of γ, we can estimate the range to the surface.

2.1.2. $\phi = 0°, \theta \neq 0°$. When ϕ is zero but θ is not, specular reflection does not affect the detector reading since the line of sight of the detector does not lie on the plane where the specularly reflected beam propagates, as shown in figure 7. Thus, the detector reading is completely dominated by the diffuse reflection component, as illustrated in figure 8. Furthermore, only the diffusely reflected beam propagating on the sensor plane is effective whereas the others propagating on other planes are not sensed. Therefore, the situation simplifies to the representation of diffuse reflection in figure 6. The detector output is again maximum at position 1
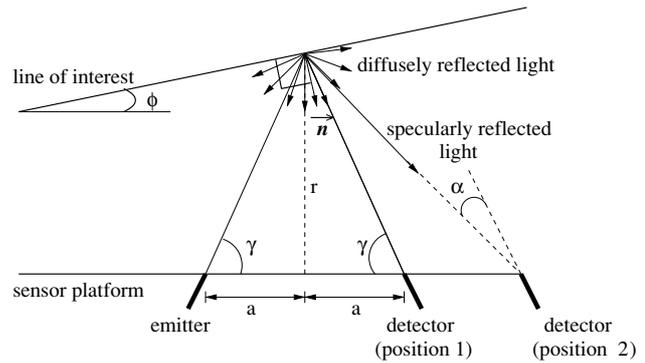

Figure 9. The cross-section of the experimental set-up.

where the detector line of sight intersects the point of reflection so that there is a component of the diffusely reflected beam in alignment with the line of sight of the detector. Hence, the distance between the linear platform and the line of interest is estimated similar to the first case, using equation (2).

2.2. Surfaces with $\phi \neq 0°$

When $\phi \neq 0°$, since the line of interest and the baseline are no longer parallel, the distance between them becomes variable. It should also be noted that similar to the $\phi = 0°$ case, the value of θ does not affect the way the range is estimated. Therefore, for this case, θ is set to zero, in order not to increase the complexity of the geometry of the experimental set-up.

The cross-section of the set-up is given in figure 9. From the very small values of ϕ (starting at about $3°$), specular reflection becomes non-detectable by the detector since, depending on the range, the specularly reflected infrared beam either reaches the detector with a large angle that remains outside the cone-like beam pattern or is spread out of the limits of the sensor platform. As this study is realized with $5°$ increments in ϕ, the effects of specular reflection for small ϕ values ($\phi \leqslant 3°$) are not considered. Therefore, what the detector senses is only the diffuse reflection component.

When $\phi \neq 0°$, estimating the range by using equation (2) has resulted in larger range errors than in the $\phi = 0°$ case which can be explained as follows. The rays within the cone-like beam pattern reach the surface at different positions and at different angles of incidence. The rays emitted close to the line of sight of the sensor have more intensity to begin with. In addition, the rays experiencing shorter distance of travel and making smaller incidence angles with the surface normal are reflected more powerfully as described by equation (1). When $\phi = 0°$, among all the rays within the cone-like beam pattern, the ray corresponding to the brightest reflection follows the path along the lines of sight of the emitter and the detector (figure 6). However, when $\phi \neq 0°$, the ray resulting in the highest intensity reflection is no longer the one travelling along the lines of sight of the sensors. It is one of the rays either to the left or to the right of the line of sight of the emitter depending on the value of ϕ. Thus, we need to add more detail to the signal reflection model, as in figure 10, where β is the additional angle between the line of sight of the emitter and the ray resulting in the most powerful reflection. Hence, apart from ϕ, β should be determined to estimate l, which is the perpendicular distance from the most powerful reflection
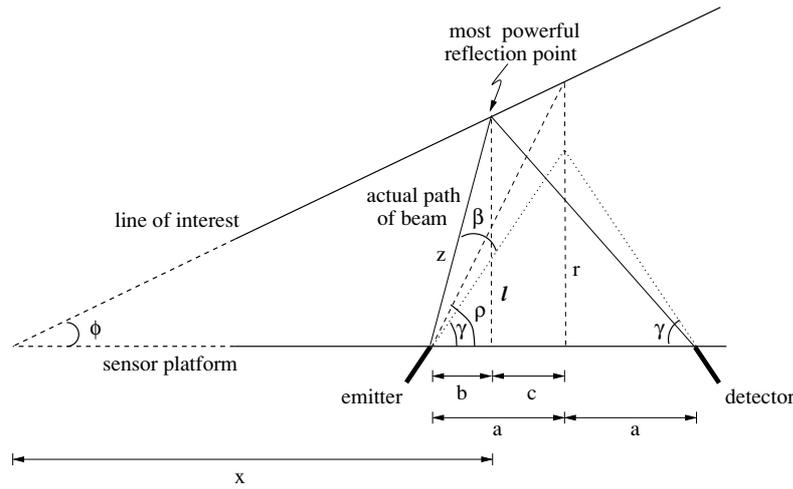
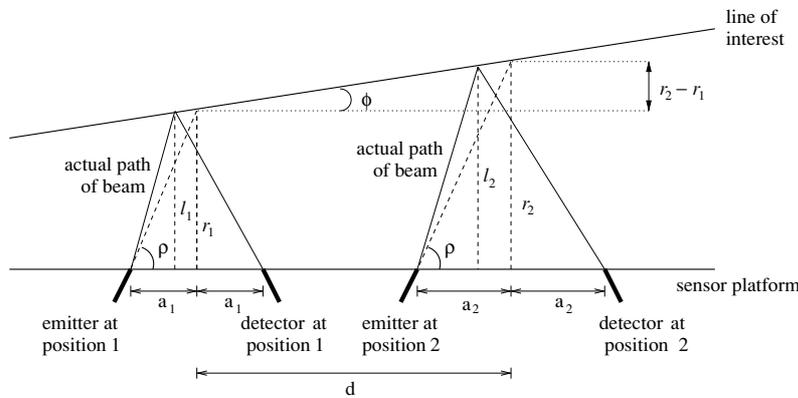**Figure 10.** The improved model of the experimental set-up.

Figure 11. Range estimation when $\phi \neq 0°$.

point to the baseline of the sensors. Note that the point where the line of length l intersects the baseline of the sensors is not the mid-point of the emitter–detector separation. The distance from the mid-point of the emitter–detector pair to the line of interest is r, corresponding to the actual range we want to estimate. ρ is the angle made between the linear platform and the line connecting the emitter and the intersection point of the line segment of length r with the line of interest. As β is fixed for a specific value of ϕ, if it can be shown that ρ is also fixed, then r can be used instead of l. The details of the proof showing that ρ is fixed for a given value of ϕ are provided in the appendix.

The fact that ρ depends only on ϕ enables us to use ρ and r instead of $(\gamma + \beta)$ and l for range estimation. This is advantageous since the line of length r intersects the baseline at the mid-point of the emitter–detector separation, whereas the position where the line of length l intersects the baseline needs computing. The ρ values are experimentally found and recorded for different ϕ values as explained later in section 3. These will be used to find ρ values for an arbitrary value of ϕ after nonlinear curve fitting to the data.

As ρ depends on ϕ, the value of ϕ should be determined first. The procedure we used can be outlined as follows. Two distinct positions of the emitter are chosen and the corresponding detector positions where maximum intensity data are observed are found as shown in figure 11. The

distances between the emitter and the detector positions are recorded as $2a_1$ and $2a_2$, and the distance between the mid-point of the first baseline separation and the mid-point of the second baseline separation is denoted as d. From the geometry, the distance between the two emitter positions is given by $d + a_1 - a_2$, and

$$r_1 = a_1 \tan \rho \qquad (3)$$

$$r_2 = a_2 \tan \rho \qquad (4)$$

$$\tan \phi = \frac{r_2 - r_1}{d} = \frac{a_2 - a_1}{d} \tan \rho \qquad (5)$$

$$\tan \rho = \frac{d}{a_2 - a_1} \tan \phi \qquad (6)$$

where r_1 is the distance from the mid-point of the emitter–detector pair to the line of interest for the first position of the emitter and r_2 is the same for the second position of the emitter. Note that although we freely choose the two positions of the emitter, the distances a_1 and a_2 and d are determined by the positions where the maximum intensities are observed, and are, in general, dependent on ϕ. To determine this dependence, the $(a_2 - a_1)/d$ data for specific ϕ values are experimentally acquired and recorded and the corresponding $\tan \rho$ values are estimated after nonlinear curve fitting to the data. The whole procedure to estimate the range r can be summarized as follows:

- If ϕ is not zero, ratio $(a_2 - a_1)/d$ is found experimentally, and the corresponding ϕ value is read off from the line fitted to the ϕ versus $(a_2 - a_1)/d$ data (figure 15).
- Once ϕ is estimated, $\tan \rho$ can be estimated by using the $\tan \rho$ versus ϕ curve (figure 16).
- After $\tan \rho$ is estimated, the range to the surface is estimated using either one of equations (3) and (4).

3. Experimental verification

3.1. Experimental set-up

The experimental set-up (figure 2) comprises a vertical linear platform, two stepper motors, two infrared sensors and a 10-bit A/D converter chip, all of which are controlled by a single PC with two parallel ports. The set-up also includes interface circuits where needed.

Both of the infrared sensors [43] used in this study include an emitter and a detector in a metal casing (figure 1). The aperture diameters of the emitter and detector are 8 mm, and the centre-to-centre separation between them is 12 mm. To use the sensors as a separate emitter–detector pair, the detector of one of the sensors and the emitter of the other are inhibited by covering them with appropriately sized opaque material. The emitter and the detector both make a predetermined angle ($\gamma = 60°$) with the platform on which they slide, as shown in figure 6.

The sensors work with 20–28 V dc input voltage, and provide an analogue output voltage proportional to the measured intensity reflected off the target. The window of the detector has been covered with an infrared filter by the manufacturer to minimize the effect of ambient light on the intensity measurements. Indeed, when the emitter is turned off, the detector reading is essentially zero. The sensitivity of the device can be adjusted with a potentiometer to set the operating range of the system. In our system, this is done automatically using a stepper motor. The detector output is interfaced to the PC after it is processed by a 10-bit microprocessor-compatible A/D converter chip having a conversion time of 100 μs and 10 mV resolution. (Initially, we used an 8-bit A/D converter chip which did not provide sufficient accuracy.) With the present configuration, the detector output ranges between 0 and 4.9 V, where saturation occurs at 4.9 V.

The linear platform constitutes the basis for the linear motion of the detector. The platform on which the detector moves up and down over a 60 cm range consists of two support rods on both sides of a 70 cm long infinite screw, all made of steel, as shown in figure 2. A 5.1 W stepper motor is directly connected to the upper end of the infinite screw so that the rotation of the stepper motor is converted to a linear motion in the vertical direction. The step size of the motor is 1.8° corresponding to 0.04 cm linear displacement of the detector at each step. To be able to record the distance between the emitter and the detector, it is sufficient to keep track of the number of steps the motor takes. Counterclockwise rotation of the stepper motor moves the detector upwards and clockwise rotation results in downward motion. A second stepper motor is directly connected to the potentiometer of the detector to set the sensitivity of the device automatically. In fact, it is

Table 1. Standard deviation values for wood and white paper at different ranges.

r (cm)	Std (V) at max intensity		Max std (V)	
	Wood	White paper	Wood	White paper
15.0	0.0046	0.0045	0.0079	0.0078
17.5	0.0052	0.0044	0.0094	0.0057
20.0	0.0053	0.0034	0.0081	0.0063
22.5	0.0059	0.0033	0.0088	0.0055

used to adjust the sensitivity of the detector when the acquired intensity data are saturated, as explained in more detail in section 3.2.

The whole system is 90 cm high and weighs around 10 kg including the sensors and the stepper motors. The overall cost of such a system is around 300 US$ including the motors but not the sensors and the PC. The system provides high precision in linear motion together with high stability.

3.2. Experimental results

First, we wanted to check the repeatability of the experimental data acquired and see if there is any significant difference between the data acquired during upward and downward motion. For this purpose, for a fixed position of the emitter, the detector slides upwards along the sensor platform to record the intensity data and the corresponding baseline separation at each step of the stepper motor. Once the upward motion is completed, the detector changes direction and slides downwards at the same sensitivity setting. In figure 12, the data acquired from a planar surface covered with white paper during the upward and downward motion are shown and it is seen that they are very close to each other except for some slight differences. Since there is no significant difference between data collected during upward and downward motion, we conclude that the data are repeatable.

In the next step, to quantify the noise fluctuations and the uncertainty of the intensity data, we collected 100 intensity data at each step of the motor and recorded the mean and the standard deviation of these data, together with the corresponding baseline separation. The results are shown in figure 13 for white paper where the mean intensity data are plotted together with ± 10 standard deviations. In table 1, standard deviation values at the maximum intensity position of the intensity scan and the maximum standard deviation value of the complete scan are tabulated at four different distances for wood and white paper. The standard deviation values do not seem to have a dependence on distance. The values for wood are, in general, larger than those obtained for white paper, possibly due to the natural patterns on wood. Since the maximum intensity that can be measured by the system corresponds to 4.9 V, it can be concluded that the standard deviation is at most 0.2% of the saturation intensity.

The procedure we used for range estimation is as follows. For a given fixed position of the emitter, the detector starts to slide upwards along the sensor platform to collect and record the intensity data and the corresponding baseline separation at each step of the stepper motor. During its motion, the detector collects 100 intensity data at each step of the stepper
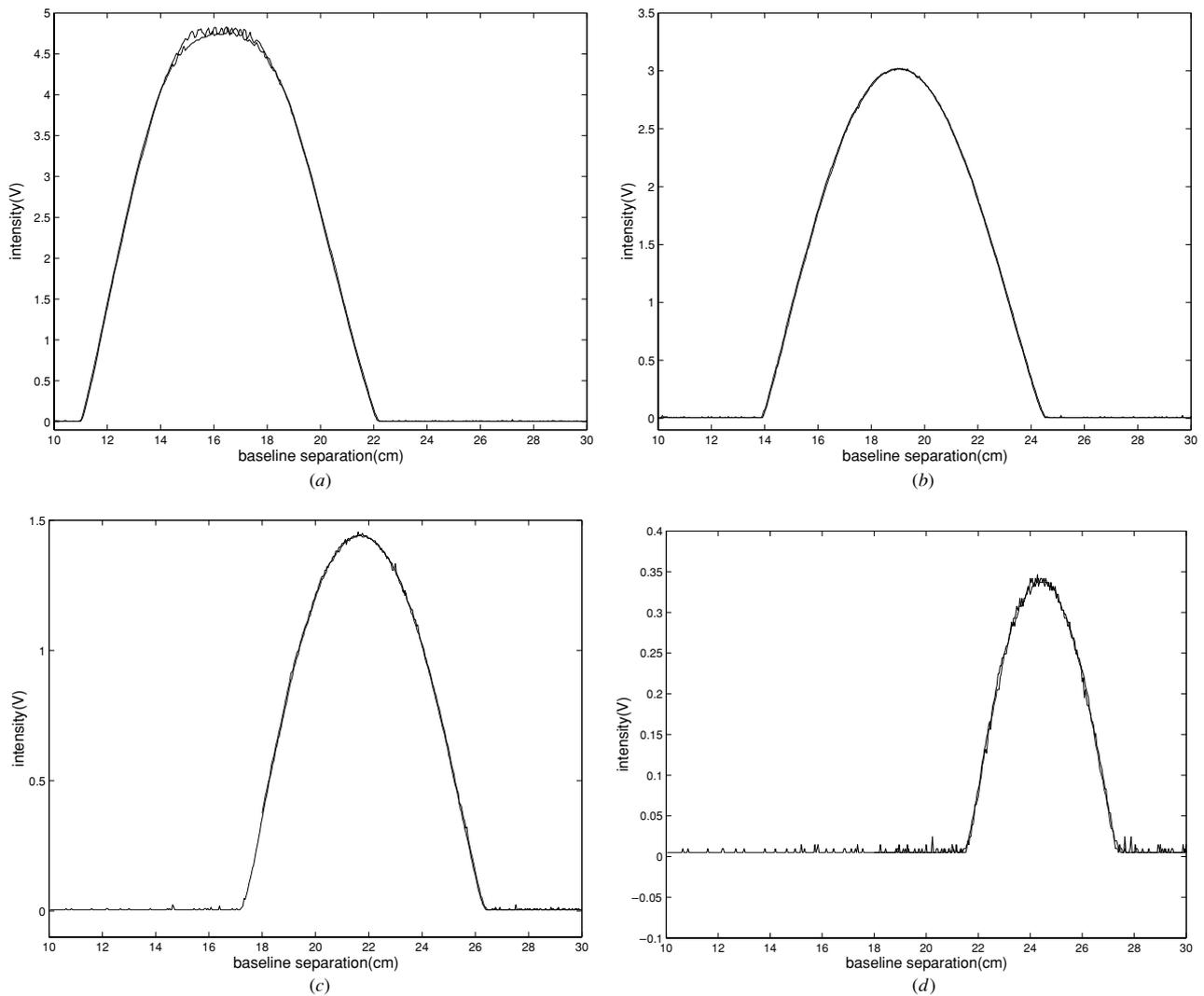
Figure 12. Data acquired during upward and downward motion for a planar surface covered with white paper at (*a*) 15 cm, (*b*) 17.5 cm, (*c*) 20 cm, (*d*) 22.5 cm.

motor and the mean of these data is recorded together with the corresponding baseline separation. As soon as the upward motion ends, the intensity data are checked for saturation. An intelligent feature of our experimental set-up is the automatic adjustment of the sensitivity of the detector to eliminate saturation. Four different sensitivity settings are available. Initially, the detector is set to the maximum sensitivity setting. If saturation is detected during the upward motion, the second stepper motor adjusts the sensitivity of the detector to a lower setting. Based on the centre of gravity of the saturated intensity data acquired during the upward motion, it is possible to make a rough estimate of the distance to the surface. Using this estimate, the sensitivity of the detector can be adjusted usually in one step and the adjusted setting is used throughout the downward motion. However, at ranges below 14.5 cm for white paper and below 14.0 cm for wood, saturation cannot be eliminated even with the minimum sensitivity setting of the detector.

As soon as the detector completes its motion, the intensity data are inspected to find the maximum intensity data and the corresponding baseline separation. These are recorded for the present position of the emitter. The procedure is repeated for a second position of the emitter, resulting in another set of position-intensity data.

The proposed method is verified experimentally. A hard planar surface of dimensions 1 m × 0.5 m × 1 cm is used which is made of unpolished oak wood of light brown colour with some natural patterns (vertical stripes as seen on the surface pictured in the left part of figure 2). The surface is either left uncovered as plain wood or covered with white paper, bubbled packing material, white Styrofoam, blue, black and red cardboard. The results are discussed in the following subsections.

3.2.1. Experimental results when $\phi = 0°, \theta = 0°$. Reference data sets are collected for each different surface, exhibiting different reflection properties, from 10 to 50 cm with 2.5 cm distance increments. For this case, as explained in section 2.1.1, it is sufficient to find the value of *a*, which is half of the baseline separation between the emitter and the detector when the detector senses the maximum intensity data. To find the value of *a*, we used three different methods of processing
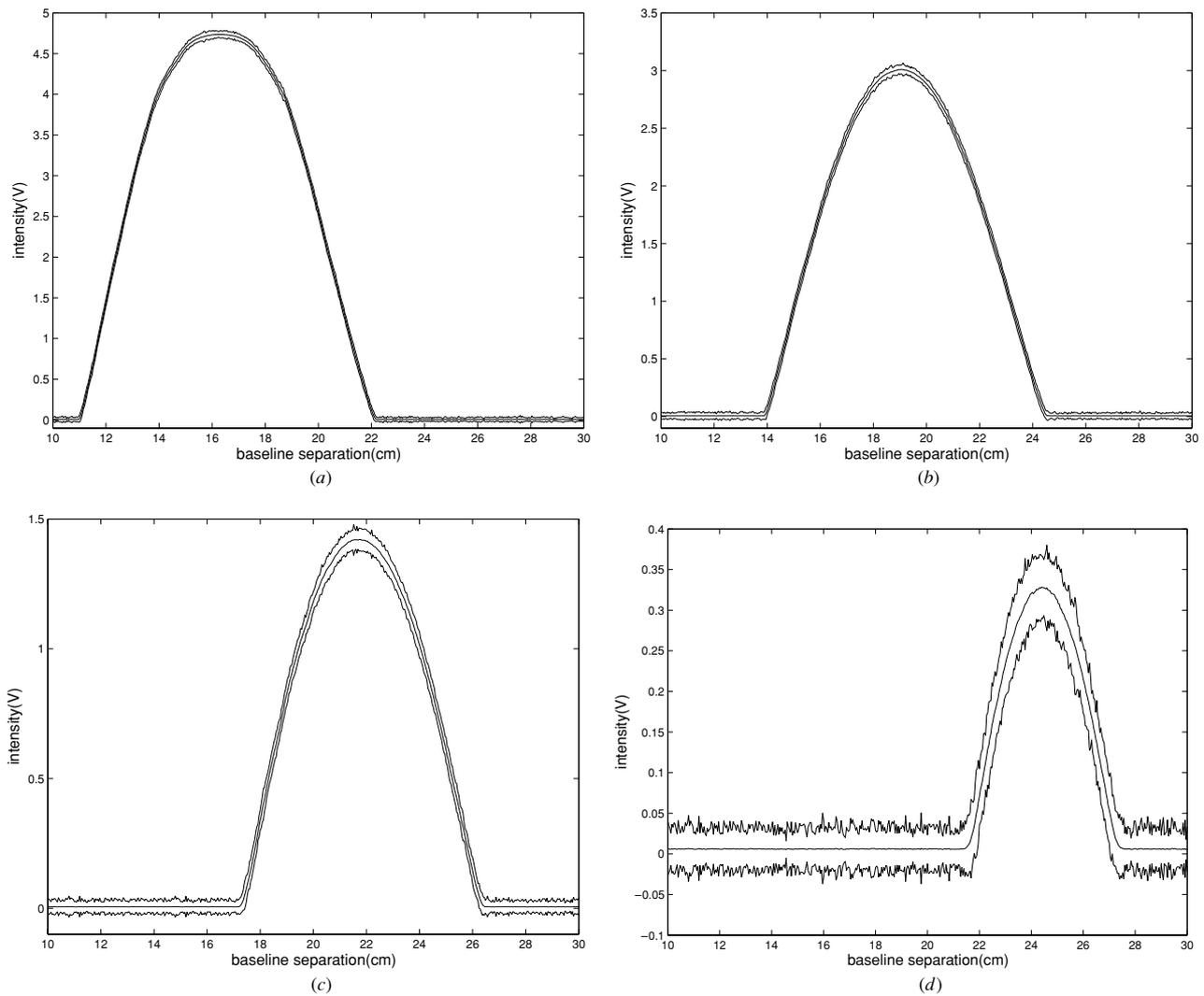
Figure 13. The mean intensity ±10 standard deviations for a planar surface covered with white paper at (*a*) 15 cm, (*b*) 17.5 cm, (*c*) 20 cm, (*d*) 22.5 cm.

the acquired intensity scan signals based on using the detector positions corresponding to (i) the maximum intensity value, (ii) the mid-point after thresholding, and (iii) the centre of gravity (COG) of the intensity curve.

In the first method, the intensity data are searched for a single maximum. If a single maximum exists, the corresponding *a* value is recorded. However, in many instances, the intensity curve may have multiple maxima; that is, the detector senses maximum intensity data at a number of positions which are not necessarily consecutive. If such multiple maxima exist, then the mean of the corresponding *a* values is calculated and used.

In the second method, the intensity data are thresholded to retain as many samples as possible from the body of the intensity curve. The value of the threshold used is, in general, different for different intensity scans. Among the intensity values exceeding the threshold, the one corresponding to the middle is found and the corresponding *a* value is recorded.

In the last method, we use the same threshold value as in the previous method for each intensity curve and find the COG of the intensity values exceeding the threshold, calculated

according to the formula

$$I_{\text{COG}} = \frac{\sum_{k \epsilon I_k \geqslant \tau} a_k I_k}{\sum_{k \epsilon I_k \geqslant \tau} a_k} \quad (7)$$

where I_k represents the intensity data sample, a_k represents half of the corresponding baseline separation, and τ is the threshold value. The *a* value corresponding to I_{COG} is recorded.

The experimental results are given in tables 2 and 3. The overall absolute mean range error using all three methods is calculated as 0.21 cm for eight different surfaces over the range from 10 to 50 cm. The errors do not tend to show any trend with increasing range. When the three methods are compared, it is seen that using the COG method gives the best results with an absolute average range error of 0.15 cm. The thresholding method results in 0.18 cm error and the maximum intensity method gives 0.30 cm error, which is less accurate than the other two. Using the maximum intensity method, the errors seem to fluctuate more compared with the other two methods. Therefore, it can be concluded that by processing more samples from the body of the intensity scan signals, the robustness of range estimation is improved.

Table 2. Range errors for four different surfaces when $\phi = 0°$ and $\theta = 0°$.

	Range error (cm)											
	Wood			White paper			White Styrofoam			Black cardboard		
True r (cm)	Max	Thld	COG	Max	Thld	COG	Max	Thld	COG	Max	Thld	COG
10.0	−0.01	0.21	0.20	0.85	0.13	0.13	0.19	0.06	0.06	−0.18	−0.01	−0.05
12.5	−0.14	0.37	0.23	−0.55	−0.21	−0.36	−0.69	0.32	0.11	0.01	−0.03	−0.03
15.0	−0.07	0.27	0.11	−0.19	0.15	0.00	−0.25	0.17	0.01			
17.5	−0.06	0.12	0.04	−0.19	−0.01	−0.10	−0.06	0.12	0.01			
20.0	−0.06	0.05	0.01	−0.10	0.01	−0.05	−0.04	0.01	−0.03			
22.5	−0.10	0.32	0.13	−0.06	0.16	0.00	−0.03	0.27	0.08			
25.0	−0.13	0.23	0.11	−0.10	0.10	−0.01	−0.10	0.16	−0.01			
27.5	−0.19	0.12	0.07	−0.11	0.01	−0.07	−0.28	0.03	−0.09			
30.0	0.27	0.25	0.18	−0.22	0.05	−0.03	−0.28	0.20	0.06			
32.5	−0.09	0.31	0.17	−0.50	−0.02	−0.08	−0.06	0.09	0.00			
35.0	0.02	0.28	0.20	−0.11	−0.13	−0.15	−0.29	0.07	0.02			
37.5	−0.31	0.29	0.19	−0.30	−0.26	−0.26	−0.24	0.07	0.04			
40.0	−0.24	0.19	0.11	−0.13	−0.26	−0.27	−0.05	0.11	0.09			
42.5	0.20	0.06	0.03	−0.50	−0.14	−0.16	0.35	0.00	−0.01			
45.0	0.28	−0.03	−0.04	−0.38	−0.34	−0.36	−0.23	−0.03	−0.04			
47.5	−0.12	−0.14	−0.14	−0.34	−0.45	−0.45	−0.27	−0.07	−0.07			
50.0	0.03	−0.14	−0.13	0.10	−0.31	−0.30	−0.16	−0.16	−0.16			
Mean error:	−0.04	0.16	0.09	−0.17	−0.09	−0.15	−0.15	0.08	0.00	−0.09	−0.02	−0.04
Absolute mean error:	0.14	0.20	0.12	0.28	0.16	0.16	0.21	0.11	0.05	0.10	0.02	0.04

Table 3. Range errors for four other surfaces when $\phi = 0°$ and $\theta = 0°$.

	Range error (cm)											
	Blue cardboard			Red cardboard			Large bubbles			Small bubbles		
True r (cm)	Max	Thld	COG	Max	Thld	COG	Max	Thld	COG	Max	Thld	COG
10.0	−0.10	0.13	0.13	0.19	0.15	0.15	0.54	0.17	0.17	−0.69	0.04	0.04
12.5	0.54	0.34	0.17	−0.29	0.25	0.09	0.37	0.54	0.41	−0.05	0.45	0.28
15.0	−0.30	0.15	−0.01	−0.19	0.17	0.04	−0.03	0.21	−0.05	0.04	0.41	0.23
17.5	−0.23	0.03	−0.10	−0.14	0.05	−0.03	−0.32	0.12	−0.19	−0.05	0.28	0.05
20.0	−0.16	−0.12	−0.16	−0.05	−0.01	−0.06	−0.25	−0.16	−0.04	−0.10	0.08	−0.01
22.5	−0.25	0.16	−0.03	−0.14	0.21	0.02	−0.03	0.23	0.03	−0.50	0.31	0.12
25.0	−0.21	0.03	−0.13	−0.28	0.09	−0.04	−0.83	0.10	−0.15	0.53	0.25	−0.02
27.5	−0.21	−0.10	−0.19	−0.32	−0.08	−0.16	0.34	0.00	−0.15	−0.35	0.09	−0.22
30.0	−0.21	0.21	0.01	−0.19	0.03	−0.05	0.38	0.25	0.11	−1.24	−0.28	−0.37
32.5	−0.28	0.13	0.02	−0.24	0.03	−0.03	−0.28	0.20	0.14	−0.22	−0.30	−0.40
35.0	−0.13	0.03	−0.02	0.13	0.11	0.10	0.90	0.07	0.08	−0.83	−0.64	−0.68
37.5	0.06	−0.02	−0.04	−0.28	0.04	0.01	0.79	−0.02	−0.02	−1.12	−0.46	−0.58
40.0	−0.09	−0.07	−0.09	−0.31	−0.02	−0.07	−0.64	0.00	−0.06	−0.94	−0.38	−0.42
42.5	0.06	−0.13	−0.15	−0.75	−0.13	−0.19	−0.90	−0.38	−0.46	0.79	−0.46	−0.42
45.0	−0.35	−0.27	−0.29	−0.50	−0.49	−0.52	−0.20	−0.51	−0.51	0.35	−0.20	−0.16
47.5	−0.97	−0.51	−0.51	−0.34	−0.45	−0.46	−1.19	−0.60	−0.61	−1.01	−0.42	−0.43
50.0	−0.75	−0.51	−0.51	0.33	0.39	0.39	−0.75	−0.62	−0.61	−1.12	−0.56	−0.56
Mean error:	−0.21	−0.03	−0.11	−0.20	0.02	−0.05	−0.12	−0.02	−0.11	−0.38	−0.11	−0.21
Absolute mean error:	0.29	0.17	0.15	0.27	0.16	0.14	0.51	0.25	0.22	0.58	0.33	0.29

3.2.2. Experimental results when $\phi = 0°, \theta \neq 0°$. When $\phi \neq 0°$, the intensity curves become significantly asymmetric. In figure 14, cases $\theta = 0°$ and $\theta \neq 0°$ corresponding to the same distance are plotted together to show how these intensity curves differ. (A small amount of asymmetry also exists in $\theta = 0°$ curves.) Therefore, if a substantial amount of asymmetry exists, it can be concluded that $\theta \neq 0°$ as long as it is known that $\phi = 0°$. Whether $\phi = 0°$ or not is determined as discussed in section 2.2. Note that in parts (*a*) and (*c*) of figure 14 which correspond to a range of 10 cm, the intensity

curves remain saturated even though the minimum sensitivity setting of the detector was used.

Measurements are collected for the wooden surface and the surface covered with white paper from 10 to 40 cm with 10 cm distance increments at values of θ ranging from 5° to 60° with 5° increments. The range estimation errors are given in tables 4 and 5 for wood and white paper, respectively, using the three methods described in the previous section. The errors start to increase for larger values of $|\theta|$ and also with increasing range. The increase of the errors with $|\theta|$
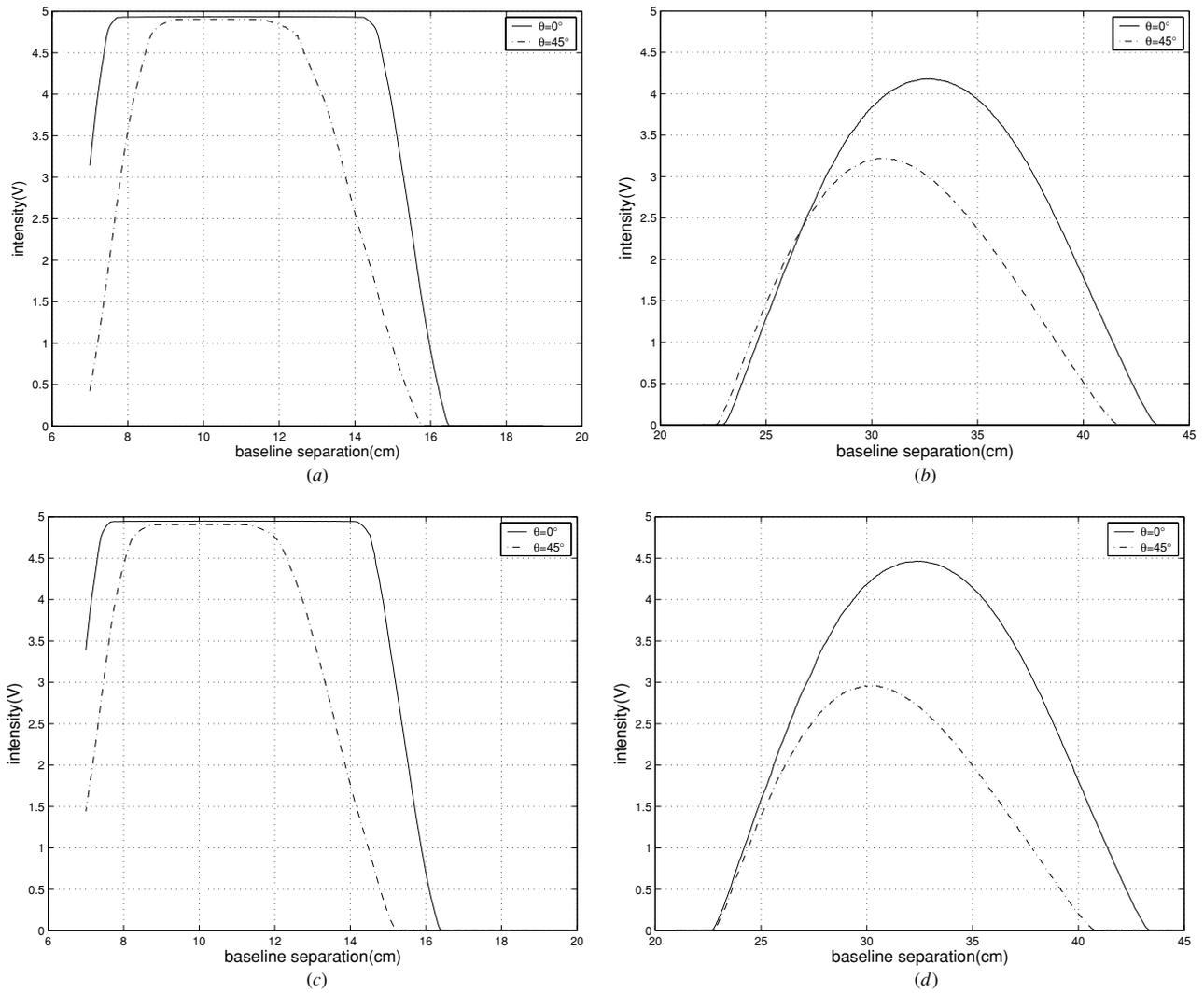
Figure 14. Intensity curves for $\theta = 0°$ and $\theta \neq 0°$. Wooden surface at (*a*) 10 cm, (*b*) 30 cm; surface covered with white paper at (*c*) 10 cm, (*d*) 30 cm.

Table 4. Range errors for wood when $\phi = 0°$ and $\theta \neq 0°$ at different ranges.

	Range error (cm)											
	($r = 10$ cm)			($r = 20$ cm)			($r = 30$ cm)			($r = 40$ cm)		
θ (deg)	Max	Thld	COG	Max	Thld	COG	Max	Thld	COG	Max	Thld	COG
5	0.01	0.17	0.16	−0.04	0.01	−0.03	−0.10	0.14	0.09	0.02	−0.11	−0.12
10	1.51	0.24	0.23	−0.06	0.03	−0.01	−0.17	0.16	0.10	−0.09	−0.11	−0.12
15	−0.14	0.28	0.25	−0.14	−0.06	−0.12	−0.21	−0.04	−0.07	−0.31	−0.13	−0.15
20	−0.09	0.28	0.25	−0.32	−0.17	−0.23	−0.46	0.34	0.06	−0.83	−0.27	−0.30
25	0.04	0.43	0.36	−0.38	−0.28	−0.32	−0.68	0.27	−0.08	−0.79	−0.40	−0.44
30	0.06	0.35	0.26	−0.50	0.27	−0.06	−1.09	0.14	−0.12	−1.56	−0.64	−0.72
35	−0.11	0.41	0.27	−0.76	0.08	−0.25	−1.38	−0.06	−0.44	−1.19	−0.86	−1.01
40	−0.34	0.39	0.20	−0.84	−0.14	−0.46	−1.62	−0.19	−0.74	−1.84	−1.47	−1.56
45	−0.69	0.28	0.04	−1.17	−0.49	−0.75	−1.88	−0.54	−1.12			
50	−0.77	0.08	−0.19	−1.52	−1.04	−1.21	−2.54	−1.20	−1.70			
55	−0.95	−0.23	−0.51	−1.68	−1.66	−1.73	−2.89	−2.25	−2.49			
60	−1.25	−0.69	−0.90	−2.38	−1.28	−1.75	−3.59	−3.15	−3.34			
Mean error:	−0.23	0.17	0.04	−0.54	−0.39	−0.58	−1.38	−0.53	−0.82	−0.82	−0.50	−0.55
Absolute mean error:	0.50	0.32	0.30	0.82	0.46	0.58	1.38	0.70	0.86	0.83	0.50	0.55

Table 5. Range errors for white paper when $\phi = 0°$ and $\theta \neq 0°$ at different ranges.

	Range error (cm)											
	($r = 10$ cm)			($r = 20$ cm)			($r = 30$ cm)			($r = 40$ cm)		
θ (deg)	Max	Thld	COG	Max	Thld	COG	Max	Thld	COG	Max	Thld	COG
5	−0.47	−0.03	−0.03	−0.17	−0.12	−0.18	−0.54	−0.32	−0.33	−0.31	−0.20	−0.24
10	0.96	0.02	0.02	−0.17	−0.08	−0.14	−0.68	−0.10	−0.18	−0.66	−0.24	−0.29
15	−0.03	0.08	0.07	−0.21	−0.10	−0.15	−0.46	−0.11	−0.22	−0.83	−0.24	−0.30
20	−0.80	0.04	0.03	−0.41	−0.21	−0.26	−0.65	−0.08	−0.22	−0.81	−0.31	−0.41
25	−0.29	0.23	0.18	−0.39	−0.30	−0.33	−0.83	−0.30	−0.42	−0.90	−0.46	−0.60
30	−0.27	0.19	0.13	−0.62	−0.58	−0.58	−0.90	−0.33	−0.40	−1.30	−0.62	−0.87
35	−1.02	0.04	−0.04	−0.69	0.07	−0.27	−1.16	−0.46	−0.59	−1.71	−1.03	−1.27
40	−0.75	−0.05	−0.16	−0.87	−0.23	−0.53	−1.46	−0.68	−0.86	−1.93	−1.78	−1.86
45	−0.84	−0.27	−0.38	−1.28	−0.63	−0.88	−1.75	−0.89	−1.16			
50	−0.99	−0.40	−0.56	−1.61	−1.13	−1.31	−2.38	−1.22	−1.68			
55	−1.25	−0.66	−0.83	−1.98	−1.88	−1.93	−2.60	−2.04	−2.35			
60	−1.54	−1.04	−1.18	−2.64	−1.90	−2.08	−3.61	−3.30	−3.41			
Mean error:	−0.61	−0.15	−0.23	−0.92	−0.59	−0.72	−1.42	−0.82	−0.99	−1.01	−0.61	−0.73
Absolute mean error:	0.77	0.25	0.30	0.92	0.60	0.72	1.42	0.82	0.99	1.01	0.61	0.73

has a similar explanation as in section 2.2 for the case with increasing $|\phi|$. At larger values of $|\theta|$, the effect described there is more enhanced and causes larger range errors.

When the three methods are compared, it is seen that the thresholding method gives the best results for $\phi \neq 0°$ case. However, the COG method gives comparable results to that of the thresholding method. As in the previous case, the maximum intensity method again gives the least accurate results.

In conclusion, the range is estimated in the same way regardless of whether $\theta = 0°$ or $\theta \neq 0°$. However, the value of θ affects the accuracy of range estimation since the range error increases with $|\theta|$.

3.2.3. Experimental results when $\phi \neq 0°, \theta = 0°$. In this case, reference data sets are collected for the wooden surface, for ϕ ranging from 5° to 45° with 5° increments. Since the detector slides over a fixed 60 cm range for each of the two positions of the emitter, and the full extent of the infinite screw is 70 cm long, the separation $(d + a_1 - a_2)$ between the emitter positions could not have been made too large in order to keep the height of the platform within reasonable limits. On the other hand, the emitter separation could not have been made too small in order to have sufficient resolution in the range measurements. Therefore, a value between 5–10 cm was a reasonable choice. The specific value used in our experiments was 6.3 cm. Using the reference data sets, $(a_2 - a_1)/d$ values are calculated applying the procedure explained in section 2.2 and the experimental data points in figure 15 are obtained. Next, ρ values are extracted for corresponding ϕ values by measuring the actual distance r and evaluating $\tan \rho = r/a$ (figure 10) and the experimental part of figure 16 is constructed. Then, least-squares curve fitting is applied to the experimentally acquired ϕ versus $(a_2 - a_1)/d$ and $\tan \rho$ versus ϕ data.

Finally, a new data set is collected to be used as test data. First, the $(a_2 - a_1)/d$ value is calculated based on the two positions where the two maximum intensities are observed. The corresponding ϕ value is estimated from the fitted line
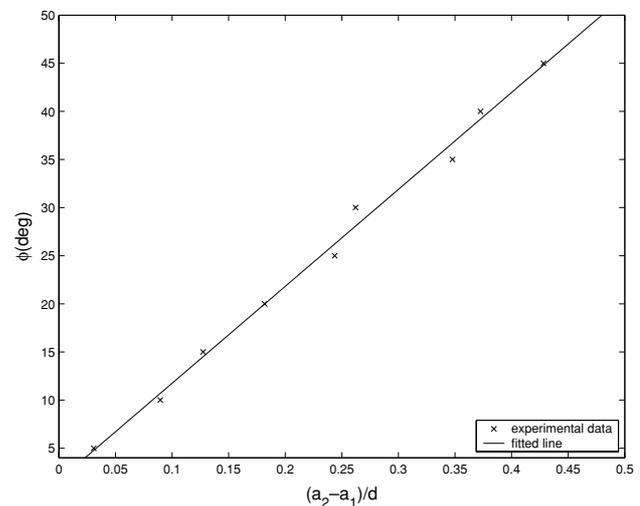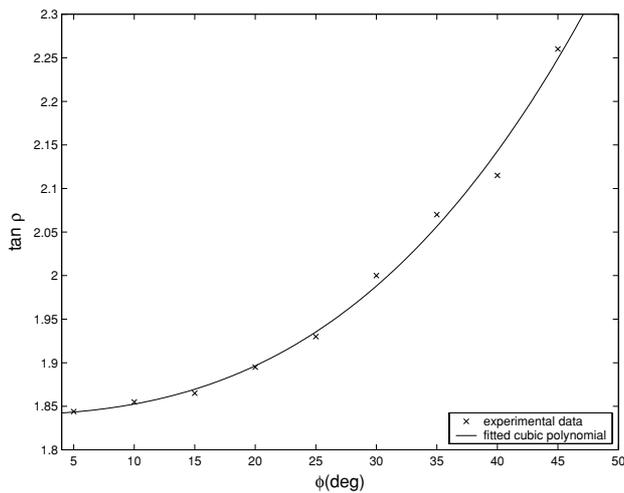

Figure 15. Experimental data for ϕ versus $(a_2 - a_1)/d$ for a wooden surface.

shown in figure 15. Then the value of $\tan \rho$ corresponding to this estimated ϕ value is found using the fitted curve in figure 16. Finally, the range to the surface is estimated using either one of equations (3) and (4). The results are tabulated in table 6. In this case, the thresholding and COG methods provide comparable results again.

3.2.4. Experimental results when $\phi \neq 0°, \theta \neq 0°$. Finally, to see the effects of θ when $\phi \neq 0°$, we collected reference data sets for the wooden surface for θ ranging from 5° to 25° with 5° increments for three values of ϕ, which are 5°, 10° and 15°. The results obtained are given in table 7. In order to see the effect of changing θ and ϕ angles clearly, here, it would be ideal to keep the value of r constant. However, since both ϕ and θ are varied, it is very difficult to maintain constant r experimentally. Therefore, we have tried to keep changes in r moderate so that r falls within the narrow range of about 30–39 cm.

Table 6. Range errors when $\phi \neq 0°$ and $\theta = 0°$ for wood.

True ϕ (deg)	ϕ error (deg)			True r (cm)	Range error (cm)		
	Max	Thld	COG		Max	Thld	COG
5	1.8	2.4	2.5	32.8	−0.24	−0.02	−0.03
				33.4	−0.21	0.09	0.07
10	−1.5	0.1	0.1	37.9	−0.36	−0.04	−0.06
				39.0	−0.61	−0.07	−0.09
15	4.5	0.9	0.9	29.3	−0.25	0.22	0.20
				31.5	0.13	−0.03	−0.05
20	1.1	0.5	0.5	30.3	−0.09	0.11	0.11
				33.1	0.01	0.08	0.08
25	−0.7	−1.7	−1.7	28.7	−0.98	0.13	0.13
				32.3	−1.03	−0.13	−0.13
30	3.9	0.4	0.4	28.8	−1.48	0.17	0.17
				33.9	−0.48	0.14	0.14
35	−1.3	−0.3	−0.3	30.1	−0.93	0.26	0.23
				36.7	−1.47	0.03	0.01
40	1.2	1.1	1.0	17.8	−1.34	0.69	0.67
				26.4	−1.01	0.96	0.91
45	1.7	4.3	4.4	12.5	−0.52	0.35	0.34
				24.8	−0.92	1.61	1.64
Mean error:	1.2	0.9	0.9		−0.65	0.25	0.24
Absolute mean error:	2.0	1.3	1.3		0.67	0.28	0.28

Figure 16. Experimental data for $\tan \rho$ versus ϕ for a wooden surface.

When the error values are investigated, it is seen that the overall accuracy here is of the same order of magnitude as that of case $\phi \neq 0°, \theta = 0°$. However, remember that in the case $\phi = 0°, \theta \neq 0°$, the error values tend to increase with increasing $|\theta|$. Therefore, it can be concluded that when both $\phi \neq 0°$ and $\theta \neq 0°$, the effects of θ being nonzero are dominated by the effects introduced by the nonzero value of ϕ. As the effects caused by nonzero ϕ value are compensated by the procedure described in section 2.2, range estimates in this case are accurate despite the effects of nonzero θ.

As expected, the maximum intensity values for this case are smaller than the values for the other cases of the same range. This is a natural result of the fact that when both ϕ and θ are nonzero, a smaller percentage of the reflected light reaches the detector. In addition, the intensity plots are observed to be significantly asymmetric as in the $\phi \neq 0°, \theta = 0°$ case.

Table 7. Range errors when $\phi \neq 0°$ and $\theta \neq 0°$ for wood.

ϕ (deg)	θ (deg)	True r (cm)	Range error (cm)		
			Max	Thld	COG
5	5	31.0	−0.07	0.26	0.26
	10	33.1	−1.13	0.16	0.16
	15	35.1	−0.57	−0.04	−0.04
	20	36.5	−0.22	0.09	0.07
	25	39.0	−0.31	0.01	0.01
10	5	30.5	−0.15	0.51	0.51
	10	33.0	−0.32	0.09	0.09
	15	35.0	−0.21	0.33	0.31
	20	36.5	−0.08	0.25	0.25
	25	38.5	−0.26	0.05	0.03
15	5	29.5	−0.04	0.45	0.45
	10	31.5	0.06	0.41	0.40
	15	34.0	0.06	0.92	0.92
	20	37.0	−0.88	−0.22	−0.24
	25	38.5	−0.64	0.39	0.39
Mean error:			−0.32	0.24	0.24
Absolute Mean error:			0.33	0.28	0.28

Therefore, in $\phi \neq 0°$ cases, the decision of θ being zero or not needs more computing or additional data. One way to handle this situation would be to use a second detector moving perpendicularly to the first one, from which additional data regarding θ could be obtained. Such a system would also be able to detect variation in depth in both the vertical and horizontal directions.

4. Conclusion and discussion

In this study, a novel method for range estimation of surfaces using infrared sensors has been described. We employ a pair

of infrared sensors mounted on a vertical linear platform on which they can be moved independently. The basic idea of our method is that the detector reading is maximum at some positions and the corresponding positional values of the sensors can be used for range estimation with suitable processing of the infrared intensity scans. To realize this idea, the detector slides along the platform to collect intensity data and these data are compared to find the maximum in magnitude for a given position of the emitter. The performance of the proposed system has been evaluated to estimate the range to the surface. The method is extended to the cases where the azimuth angle θ and the elevation angle ϕ are nonzero. Three different methods of processing the infrared intensity scans have been considered. The method that gives the most accurate results is based on finding the centre of gravity of the infrared intensity scans. In this case, the mean absolute range error achieved is calculated as 0.15 cm over the range from 10 to 50 cm.

The experimental results obtained show that the developed system is successful in localizing planar surfaces to an unexpectedly high accuracy without prior knowledge of their surface characteristics. Instead of employing an emitter and a detector in linear motion, one can further improve the speed of the system with the use of two fixed emitters and an array of infrared detectors. This would also simplify the system considerably. The system developed here is a prototype demonstrating that the range estimation method we propose indeed works and provides accurate range estimates using simple infrared sensors.

The main contribution of this study is that the proposed method is relatively independent of the type of surface encountered since it is based on searching for the maximum value of the intensity rather than using absolute intensity values for a given surface which would depend on the surface properties. The system can be viewed as a variable triangulation system tuned to maximum intensity data. However, the type of surface inevitably affects the range of distances over which intensity data are available and affects the operating range of the system. Therefore, as long as intensity data from a surface are available over a given range of detector positions, range is estimated relatively independently of the surface type.

An equivalent system could have been implemented by keeping the linear positions of the emitter and the detector fixed but acquiring an intensity scan by rotating the detector. In this case, the intensity scans acquired would be angular scans rather than scans obtained through linear motion. Then, the range can be estimated in a similar way by searching for the maximum intensity of the angular scans so obtained.

Our current and future works involve improving the system performance when the azimuth angle θ is nonzero. Estimating the value of angle θ accurately will enable our system to be used in map building of unknown indoor environments. One way to increase the accuracy of angular position estimation would be to include a second detector in the system moving perpendicularly to the first one. This would provide an additional dimensionality to the present system.

In this study, we considered position estimation of planar surfaces. A related future research direction is to extend the position estimation method developed here to other

geometries frequently encountered in indoor environments such as corners, edges and cylinders. Recognition of different surface types or discontinuities in the surface characteristics is another problem to be addressed.

Appendix

From the geometry of figure 10,

$$b = \frac{l}{\tan(\gamma + \beta)} = z\cos(\gamma + \beta) \tag{A1}$$

$$x = \frac{l}{\tan\phi}. \tag{A2}$$

Applying the sine law to the triangle formed by the emitter, detector and the reflection point, and extracting z to the left hand side,

$$z = \frac{2a\sin\gamma}{\sin[180° - (2\gamma + \beta)]}. \tag{A3}$$

Combining equations (A1) and (A3),

$$b = \frac{2a\sin\gamma\cos(\gamma + \beta)}{\sin[180° - (2\gamma + \beta)]}. \tag{A4}$$

Using equations (A1) and (A4),

$$a = \frac{l\sin[180° - (2\gamma + \beta)]}{2\sin\gamma\cos(\gamma + \beta)\tan(\gamma + \beta)}. \tag{A5}$$

From the geometry of figure 10, we have

$$c = a - b \tag{A6}$$

$$\tan\rho = \frac{r}{a}. \tag{A7}$$

Combining equations (A6), (A5) and (A1),

$$c = \frac{l}{\tan(\gamma + \beta)}\left(\frac{\sin[180° - (2\gamma + \beta)]}{2\sin\gamma\cos(\gamma + \beta)} - 1\right). \tag{A8}$$

From the geometry of figure 10,

$$r = (x + c)\tan\phi = l + c\tan\phi. \tag{A9}$$

Substituting for c from equation (A8),

$$r = l\left[1 + \frac{\tan\phi}{\tan(\gamma + \beta)}\left(\frac{\sin[180° - (2\gamma + \beta)]}{2\sin\gamma\cos(\gamma + \beta)} - 1\right)\right]. \tag{A10}$$

Substituting for r and a in equation (A7) and cancelling the l term which is common in the numerator and the denominator,

$$\tan\rho = \frac{1 + \frac{\tan\phi}{\tan(\gamma+\beta)}\left(\frac{\sin[180°-(2\gamma+\beta)]}{2\sin\gamma\cos(\gamma+\beta)} - 1\right)}{\frac{\sin[180°-(2\gamma+\beta)]}{2\sin\gamma\cos(\gamma+\beta)\tan(\gamma+\beta)}}. \tag{A11}$$

Hence, given that γ is constant, equation (A11) verifies that ρ is dependent only on ϕ and β. This enables us to use ρ and r instead of $\gamma + \beta$ and l for range estimation.

References

[1] Novotny P M and Ferrier N J 1999 Using infrared sensors and the Phong illumination model to measure distances *Proc. IEEE Int. Conf. on Robotics and Automation (Detroit, MI, 10–15 May)* vol 2 (Piscataway, NJ: IEEE) pp 1644–9

[2] Benet G, Blanes F, Simó J E and Pérez P 2002 Using infrared sensors for distance measurement in mobile robots *Robot. Auton. Syst.* **40** 255–66

[3] Phong B T 1975 Illumination for computer generated pictures *Commun. ACM* **18** 311–7

[4] Genovese V, Guglielmelli E, Mantuano A, Ratti G, Sabatini A M and Dario P 1995 Low-cost, redundant proximity sensor system for spatial sensing and color-perception *Electron. Lett.* **31** 632–3

[5] Sabatini A M, Genovese V, Guglielmelli E, Mantuano A, Ratti G and Dario P 1995 A low-cost composite sensor array combining ultrasonic and infrared proximity sensors *Proc. IEEE/RSJ Int. Conf. on Intelligent Robots and Systems (Pittsburgh, PA, 5–9 Aug.)* vol 3 (Piscataway, NJ: IEEE) pp 120–6

[6] Flynn A M 1988 Combining sonar and infrared sensors for mobile robot navigation *Int. J. Robot. Res.* **7** 5–14

[7] Barberá H M, Skarmeta A G, Izquierdo M Z and Blaya J B 2000 Neural networks for sonar and infrared sensors fusion *Proc. 3rd Int. Conf. on Information Fusion (France, 10–13 July)* vol 2 pp 18–25

[8] Chen B and Tugnait J K 2000 Multisensor tracking of a maneuvering target in clutter using IMMPDA fixed-lag smoothing *IEEE Trans. Aerosp. Electron. Syst.* **36** 983–91

[9] Chen Y M and Huang H C 2000 Fuzzy logic approach to multisensor data association *Math. Comput. Simul.* **52** 399–412

[10] Cheung E and Lumelsky V J 1989 Proximity sensing in robot manipulator motion planning: system and implementation issues *IEEE Trans. Robot. Autom.* **5** 740–51

[11] Hand A J 1998 Infrared sensor counts insects *Photonics Spectra* **32** 30–1

[12] Hashimoto K, Kawaguchi C, Matsueda S, Morinaka K and Yoshiike N 1998 People counting system using multisensing application *Sensors Actuators* A **66** 50–5

[13] Butkiewicz B 1997 Position control system with fuzzy microprocessor AL220 *Lecture Notes in Computer Science* 1226 (Berlin: Springer) pp 74–81

[14] Kim H-H, Ha Y-S and Jin G-G 2003 A study on the environmental map building for a mobile robot using infrared range-finder sensors *Proc. IEEE/RSJ Int. Conf. on Intelligent Robots and Systems (Las Vegas, NV, 27–31 Oct.)* (Piscataway, NJ: IEEE) pp 711–6

[15] Everett H R 1995 *Sensors for Mobile Robots, Theory and Application* A K Peters, Ltd, 289 Linden St, Wellesley, MA

[16] Lumelsky V J and Cheung E 1993 Real-time collision avoidance in teleoperated whole-sensitive robot arm manipulators *IEEE Trans. Syst. Man Cybern.* **23** 194–203

[17] Beccari G, Caselli S and Zanichelli F 1998 Qualitative spatial representations from task-oriented perception and exploratory behaviors *Robot. Auton. Syst.* **25** 147–57

[18] Warszawski A, Rosenfeld Y and Shohet I 1996 Autonomous mapping system for an interior finishing robot *J. Comput. Civ. Eng.* **10** 67–77

[19] Lopes E P, Aude E P L, Silveria J T C, Serderia H and Martins M F 2001 Application of a blind person strategy for obstacle avoidance with the use of potential fields *Proc. IEEE Int. Conf. on Robotics and Automation (Seoul, South Korea, 21–26 May)* vol 3 (Piscataway, NJ: IEEE) pp 2911–6

[20] Klysubun P, Indebetouw G, Kim T and Poon T C 2000 Accuracy of three-dimensional remote target location using scanning holographic correlation *Opt. Commun.* **184** 357–66

[21] Esteve-Taboada J J, Refregier P, Garcia J and Ferreira C 2002 Target localization in the three-dimensional space by wavelength mixing *Opt. Commun.* **202** 69–79

[22] Wikle H C, Kottilingam S, Zee R H and Chin B A 2001 Infrared sensing techniques for penetration depth control of the submerged arc welding process *J. Mater. Process. Technol.* **113** 228–33

[23] Korba L, Elgazzar S and Welch T 1994 Active infrared sensors for mobile robots *IEEE Trans. Instrum. Meas.* **43** 283–7

[24] Hashimoto K, Tsuruta T, Morinaka K and Yoshiike N 2000 High performance human information sensor *Sensors Actuators* A **79** 46–52

[25] Yoshiike N, Morinaka K, Hashimoto K, Kawaguri M and Tanaka S 1999 360 degrees direction type human information sensor *Sensors Actuators* A **77** 199–208

[26] Andò B and Graziani S 2001 A new IR displacement system based on noise added theory *Proc. 18th IEEE Instrumentation and Measurement Technology Conf. (Budapest, Hungary, 21–23 May)* vol 1 (Piscataway, NJ: IEEE) pp 482–5

[27] de Groot P J, Postma G J, Melssen W J and Buydens L M C 2002 Validation of remote, on-line, near-infrared measurements for the classification of demolition waste *Anal. Chim. Acta* **453** 117–24

[28] Scott D M 1995 A two-colour near-infrared sensor for sorting recycled plastic waste *Meas. Sci. Technol.* **6** 156–9

[29] Phillips P J 1998 Matching pursuit filters applied to face identification *IEEE Trans. Image Process.* **7** 1150–64

[30] Pavlidis I, Symosek P, Fritz B, Bazakos M and Papanikolopoulos N 2000 Automatic detection of vehicle occupants: the imaging problem and its solution *Mach. Vis. Appl.* **11** 313–20

[31] Kwon H, Der S Z and Nasrabadi N M 2002 Adaptive multisensor target detection using feature-based fusion *Opt. Eng.* **41** 69–80

[32] Tsao T and Wen Z Q 2002 Image-based target tracking through rapid sensor orientation change *Opt. Eng.* **41** 697–703

[33] Jain A K, Ratha N K and Lakshmanan S 1997 Object detection using Gabor filters *Pattern Recognit.* **30** 295–309

[34] Zalevsky Z, Mendlovic D, Rivlin E and Rotman S 2000 Contrasted statistical processing algorithm for obtaining improved target detection performances in infrared cluttered environment *Opt. Eng.* **39** 2609–17

[35] Tag P M, Bankert R L and Brody L R 2000 An AVHRR multiple cloud-type classification package *J. Appl. Meteorol.* **39** 125–34

[36] Bhanu B, Symosek P and Das S 1997 Analysis of terrain using multispectral images *Pattern Recognit.* **30** 197–215

[37] Aytaç T and Barshan B 2002 Differentiation and localization of targets using infrared sensors *Opt. Commun.* **210** 25–35

[38] Barshan B and Aytaç T 2003 Position-invariant surface recognition and localization using infrared sensors *Opt. Eng.* **42** 3589–94

[39] Aytaç T and Barshan B 2004 Simultaneous extraction of geometry and surface properties of targets using simple infrared sensors *Opt. Eng.* **43** 2437–47

[40] Aytaç T and Barshan B 2003 Rule-based target differentiation and position estimation based on infrared intensity measurements *Opt. Eng.* **42** 1766–71

[41] Aytaç T and Barshan B 2005 Surface differentiation by parametric modeling of infrared intensity scans *Opt. Eng.* **44** at press

[42] Born M and Wolf E 1980 *Principles of Optics* (Oxford: Pergamon)

[43] Matrix Elektronik 1995 *IRS-U-4A Proximity Switch Datasheet* AG, Kirchweg 24 CH-5422 Oberehrendingen, Switzerland